

PSPMT and Photodiode Designs of a Small Scintillation Camera for Imaging Malignant Breast Tumors

Craig S. Levin, *Member, IEEE*, Edward J. Hoffman, *Senior Member, IEEE*,
Martin P. Tornai, *Student Member, IEEE*, and Lawrence R. MacDonald, *Student Member, IEEE*

Division of Nuclear Medicine and Biophysics, UCLA School of Medicine
Los Angeles, CA 90095-6948

Abstract

We are investigating the concept of utilizing a small gamma ray scintillation camera to help identify and localize malignant breast tumors after a suspicious finding in a mammogram. Excellent sensitivity and specificity for malignant breast tumors has been achieved using conventional nuclear medicine scintillation cameras with certain ^{99m}Tc labeled radiopharmaceuticals. However, because of the large size, low image resolution and high cost of these devices, they are not ideal for use in breast imaging in a mammography suite. A dedicated miniaturized camera would allow imaging at angles that are physically impossible with the standard camera. These lateral views would not include the background activity from the heart and liver. In addition, with a potentially higher intrinsic resolution, shorter collimator and if breast compression is applied, a small camera could significantly improve the sensitivity and signal to noise ratio for the scintillation imaging method. We are exploring two different photodetector technologies for a small prototype camera development. The first uses a position sensitive photomultiplier (PSPMT) as the photodetector, the second, an array of silicon PIN photodiodes (PD). In this report, we present imaging results obtained with a NaI(Tl)-PSPMT design, and the design features, expected performance and relevant energy and position measurements obtained for a test CsI(Tl)-PD device.

I. INTRODUCTION

Mammography is accepted as the best means of screening for non-palpable breast cancer. However, while the sensitivity of mammography is on the order of 85% for detecting signatures of breast cancer, those signatures are only 20-30% specific to malignancy. The result is a 70-80% rate of false positives [1-3] and a large number of unnecessary biopsies. Recent reports [4-11] on detection of malignant breast tumors using ^{99m}Tc -Sestamibi and Methylene Diphosphonate (MDP) all give sensitivities and specificities of 90% or better. We believe it would be possible to take advantage of this high sensitivity and specificity to reduce the number of unnecessary biopsies if an appropriate scintillation camera were available in or near the mammography suite. Unfortunately, because of its size (~50-70 cm across), the standard scintillation camera is not ideal for breast imaging, particularly in the confined area of a mammography suite. One study [10] has shown that a portion of the roughly 10% of lesions missed in ^{99m}Tc -Sestamibi studies cited above can be explained by either a small size and/or lower isotope uptake of the particular lesions, tissue attenuation or myocardial background. Such problems could be remedied in part by a dedicated small, higher

resolution camera which can image the breast in close proximity at angles that avoid unnecessary body background.

Our test device has a 6 cm x 6 cm field of view (FOV), a size compatible with standard mammography fixtures for compressing and immobilizing breasts during tumor localization or core biopsy. Ideally, the placement of the camera over a lesion would be guided by mammography. If the camera is used in conjunction with breast compression, the resolution and signal-to-noise ratio (SNR) should be better than that attainable with conventional scintillation cameras due to less gamma ray attenuation. Once the utility is verified, larger versions could be built for full breast imaging.

We are exploring two photodetector technologies for this investigation of small scintillation cameras. Both schemes are essentially a miniaturization of the gamma ray camera concept [12]. The first design employs a NaI(Tl) crystal coupled to a Position Sensitive Photomultiplier Tube (PSPMT). The second uses CsI(Tl) coupled to silicon PIN photodiodes (PD).

Other work on small camera development for breast imaging has been reported. Designs that use planar coincidence detection of Positron Emission Tomography (PET) radiopharmaceuticals, such as F-18 Fluorodeoxyglucose, for breast and axillary lymph node imaging have been proposed [13-15]. The design of a CsI(Tl)-mercuric iodide array for ^{99m}Tc -Sestamibi breast imaging has also been described [16]. Small gamma ray cameras based on PSPMT technology have been under development by others for medical imaging, radiation monitoring and astrophysical applications [17-20]. Small cameras based on CsI(Tl)-PD technology have been described [21,22] for use in astrophysics.

The attractiveness of the PD design is in part due to its potential for compactness and low cost [23]. For a 6 cm x 6 cm FOV, including readout electronics and background shielding, the CsI(Tl)-PD camera dimensions would be roughly 8 cm x 8 cm x 6 cm. The corresponding size for a PSPMT camera is, perhaps, 10 cm x 10 cm x 15-20 cm. The compactness of the solid state design is ideal for breast imaging. Also attractive is the seemingly inevitable reduction in the cost of silicon-based products. As a final note, the silicon Avalanche Photodiode (APD) is also ideal to readout CsI(Tl). However, to date, no reliable APD array is available.

II. METHODS

A. The PSPMT Camera Design

We have built and are currently testing and optimizing a small scintillation camera comprising a 6 cm x 6 cm x 6 mm thick NaI(Tl) crystal coupled to a Hamamatsu R3941 PSPMT. We performed Monte Carlo studies using the DETECT optical photon tracking code [24] to determine the optimal crystal

surface treatments and reflectors. The best uniformity in both resolution and sensitivity were obtained with the following conditions: (1) Top of crystal (where photons enter): fine ground and painted with a white diffuse reflector; (2) Sides of crystal: polished and painted black (absorbing); (3) Bottom of crystal (in contact with PSPMT): polished. These conditions are consistent with those for conventional gamma ray cameras [25]. A hermetically sealed NaI(Tl) crystal was acquired with the optimal surface treatments, a 3 mm glass window and a 0.5 mm thick aluminum housing.

The R3941 PSPMT has an alkali photocathode active area of 77 mm x 77 mm, 16 stage fine mesh dynode structure, and a 16 x 18 cross wire anode with 3.7 mm pitch. The inner 60 mm x 60 mm area is the most useful area of the tube in terms of its linearity. The PSPMT was selected for high photocathode uniformity (maximum variation of 3:1). The NaI(Tl) crystal and the PSPMT were optically coupled with silicon-based grease. The tube was run with a voltage of -1250 V on the photocathode. When a gamma ray interacts in the crystal, the scintillation light created will be spread within the NaI(Tl) crystal (index of refraction, $n = 1.85$), the 3 mm glass window ($n = 1.5$) of the crystal housing, and the 3 mm glass entrance window of the PSPMT. The light sharing among all of the anode wires facilitates the positioning of scintillation events in this technique. Charge spread for the mesh dynode design is significant and results in unwanted inter-channel crosstalk.

The PSPMT was read out using standard resistive charge division which multiplexes the 34 cross wire anode channels into 4 signals, designated as X+, X-, Y+, and Y-. Those signals were read out individually through a four channel line driver/preamplifier board, and shaped, amplified (NIM ORTEC 855 Spectroscopy Amplifiers, 1.5 μ s shaping time) and digitized (CAMAC BiRa 5907 Transient Digitizer). The sum of the four analog signals was used for the timing (CANBERRA 2035A Timing SCA) of the gate (ORTEC 416A Gate and Delay Generator) used to trigger the ADCs. The data acquisition is controlled via GPIB by LabView (National Instruments) and a Macintosh IIfx. The four digitized values are collected in list mode for post-processing. The position of an event in a given direction (X or Y) is then determined by a weighted mean of the signals.

The camera was characterized using both ^{57}Co (122, 136 keV) and $^{99\text{m}}\text{Tc}$ (140 keV) gamma ray sources. We measured an intrinsic energy resolution of 14.1% FWHM at 122 keV, using a non-collimated ^{57}Co point source placed directly on the 6 cm x 6 cm NaI(Tl) crystal coupled to the PSPMT. Intrinsic position uniformity and resolution was measured by stepping a 1.2 mm slit source across the face of the camera in both the X and Y directions. The slit source was formed with two 2.0 cm thick lead bricks spaced 1.2 mm apart. 6 cm x 6 cm square sections of various thickness were machined out of a standard low energy, high resolution (~1.3 mm diameter, 4 cm long hexagonal-hole) collimator and fixed to the top of the NaI(Tl)-PSPMT device. We characterized the high resolution imaging capabilities of the camera using $^{99\text{m}}\text{Tc}$ and two types of phantoms: (1) a gamma ray transmission phantom created by cutting the letters U-C-L-A in Styrofoam for a CerrobendTM mold (CerrobendTM is a high atomic number, gamma-ray absorbing material with a very low melting point, normally used to create custom shielding for radiation therapy). The nominal letter line widths were 1.5 mm; (2) a "miniature

monkey brain phantom" slice, made from cutting out the contours of a miniaturized image of a monkey brain in Lucite. A 1.5 mm thick plastic bottom was coupled to this mask and the contours were filled with $^{99\text{m}}\text{Tc}$ to simulate a small, complex isotope distribution with a uniform uptake. We acquired the image with the brain slice phantom on top of the chosen collimator.

We also investigated the use of an array of small, discrete, parallel piped crystals coupled to the PSPMT instead of one large, continuous crystal. This segmented crystal scheme has two obvious advantages over the large, continuous crystal design: (1) A gamma ray photoabsorption within a given individual crystal in the array will create scintillation photons that will be confined to that crystal and focused onto a small spot on the PSPMT face. Since fewer anode wires would be involved for positioning, this would improve the SNR compared to sharing the light among many anode wires; (2) Because the light transmission properties are approximately identical for all crystals within the segmented array, the positioning will be linear up to the edge of the FOV, unlike in the continuous crystal scheme. Gain balancing will still be necessary due to inherent intercrystal light yield variations. Disadvantages of the discrete crystal design compared to the continuous crystal design are (1) its lower sensitivity (due to the dead area between crystals); (2) the resolution is determined by the size of the crystal; higher resolution requires smaller crystals, and, therefore more crystals are required in the array to cover the same area. Also, with narrower crystals light transmission degrades; (3) a matching square hole collimator might be necessary; (4) the images created will be pixellated which implies that either linear interpolation, smoothing, or detector sub-sampling may be necessary to deal with pixellation artifacts; and (5) it is more expensive.

B. The PD Camera Design

We also are exploring the possibility of using CsI(Tl) coupled to an array of PDs for the small camera. The potential use of solid state photodetectors allows further compactness for the imaging device. If PDs are used as photodetectors, CsI(Tl) is the ideal scintillator since it has an excellent emission spectrum match to the absorption spectrum of silicon (~75% QE at 530 nm). In addition, CsI(Tl) has 35% higher light yield than NaI(Tl) and a 65% higher stopping power at 140 keV. The higher stopping power allows the use of thinner crystals, improving light spread localization and transmission, with no loss in sensitivity. Table 1 gives some properties of CsI(Tl) and NaI(Tl). CsI(Tl) crystals are relatively non-hygroscopic, making them much easier to handle, and no glass window is required. Compared to a PMT, the photodiode is more compact, has potentially smaller spacing between photodetectors and over a factor of 3 higher quantum efficiency. These features of the CsI(Tl)-PD combination could potentially give this design a comparable sensitivity and energy resolution to the NaI(Tl)-PSPMT scheme. The PMT, however, has a clear advantage in regards to noise and gain.

Table 1. Properties of NaI(Tl) and CsI(Tl) scintillation crystals.

Scintillator	Effective Z	Density (g/cc)	Radiation Length (mm) (140 keV)	Relative Light Yield	Refractive Index	Decay Time (ns)	Peak Emission Wavelength (nm)	Hygroscopic?	Rugged?
NaI(Tl)	51	3.67	3.4	100	1.85	230	410	yes	no
CsI(Tl)	54	4.51	2.2	135	1.79	1000	530	no	yes

For any PD-preamplifier combination, for the optimum SNR at the preamplifier input, the PD terminal capacitance is kept to a minimum. In addition, the PD leakage current generally increases with area. These facts, combined with the merit of using arrays of small crystals, as discussed at the end of Section IIA, imply that the best SNR for a CsI(Tl)-PD imaging array is achieved when it is composed of tiny (≤ 2 mm) CsI(Tl) crystals coupled to correspondingly small PD array elements. However, to cover a 6 cm x 6 cm area with such a highly pixellated PD array requires a customized and expensive readout. In addition, it would require a mosaic of several PD arrays to cover that large an area which would introduce significant dead regions between arrays. Finally, a custom-made square hole collimator might be required to match the crystal sizes chosen. Therefore, our initial investigation will study a coarse PD array composed of individual, large area (~ 10 mm x 10 mm) elements. We will determine whether or not this "simple" design has sufficient SNR for high resolution imaging and, if not, adjust the design (e.g. reduce the PD pixel size).

A schematic for the "simple" device is shown in Figure 1. It utilizes a 5 x 5 array of 10 mm x 10 mm area PDs with 2 mm spacing between. Both continuous and discrete CsI(Tl) crystal array designs are shown. A light guide is used to distribute light over the coarse array of PDs. The PDs for the initial array we are proposing (Hamamatsu S3590) are readily available so that no custom PD array is necessary.

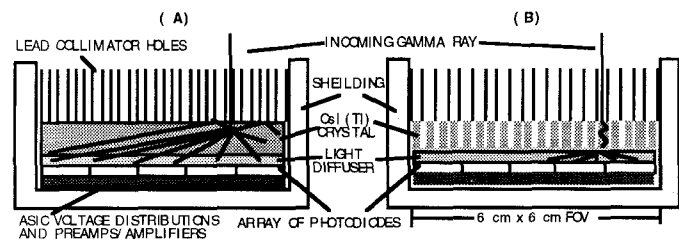


Figure 1. Schematic of the "simple" photodiode designs of a small, compact, gamma-ray scintillation camera for breast imaging. (a) Single continuous crystal. (b) Array of discrete crystals. The light spread distribution (rays) from a scintillation event within the CsI(Tl) is shown schematically for the two crystal schemes. Total dimensions: 8x8x6 cm³, including background shielding.

Monte Carlo simulations were performed using DETECT optical photon tracking code for the continuous crystal design (Fig. 1a). A 140 keV gamma ray interaction in CsI(Tl) produces approximately 7300 photons with a peak emission wavelength of 530 nm. These optical photons were tracked and optimal crystal surface treatments and reflectors were determined. A PD quantum efficiency of 75% was assumed. The best uniformity in resolution and sensitivity was obtained with the same surface treatments as found for the NaI(Tl) (see previous section). Under these optimal conditions, light tracking simulations were then used to determine camera characteristics, such as, the light transmission, the thickness of the light diffuser, the light spread width, the positioning linearity and resolution, and depth of interaction effects.

Energy measurements were made with various gamma ray sources and a small 2x2x10 mm³ CsI(Tl) crystal coupled to one of the proposed PDs. The crystal was wrapped in 5 layers of teflon and coupled to the PD with optical grease. The PD was read out with a charge sensitive preamplifier (ORTEC 142A), a shaping amplifier (CANBERRA 2021, gaussian,

1.5 μ s shaping time) and digitized. ⁵⁷Co, ²²Na and ¹³⁷Cs gamma ray sources were used for these measurements.

In order to assess the imaging potential of the continuous CsI(Tl)-PD combination proposed, we used a 23 mm x 10 mm x 4 mm CsI(Tl) crystal, two PDs, and uncollimated gamma ray sources. The crystal was wrapped (top and sides) in 5 layers of teflon tape and coupled to the two PDs with optical grease. The PDs were attached to two available charge sensitive preamplifiers (ORTEC 142A and 109A). A 1-D weighted mean of the two PD signals determined the location of a gamma ray interaction.

III. RESULTS

A. The PSPMT Positioning Linearity, Resolution, and Imaging Capabilities

Figure 2 and 3 shows the results of stepping a 1.2 mm ⁵⁷Co slit source across the face of the NaI(Tl)-PSPMT device in 5 mm steps. Figure 2a displays the ratio positioning response in the x and y-directions. The extent of the linearity and dynamic range appear to give a central 5 x 5 cm useful FOV. Figure 2b shows the Line Spread Functions (LSFs) across the FOV in the x-direction. The FWHM spread of the LSF is a measure of the camera's intrinsic resolution. The mean, standard deviation and range (max-min) of the FWHMs are, respectively, 2.6, 0.1 and 0.5 mm in the x-direction and 2.5, 0.2, and 0.6 mm in the y-direction. A simple deconvolution of the source size yields 2.2 mm FWHM for the mean intrinsic resolution in the y-direction. This resolution is

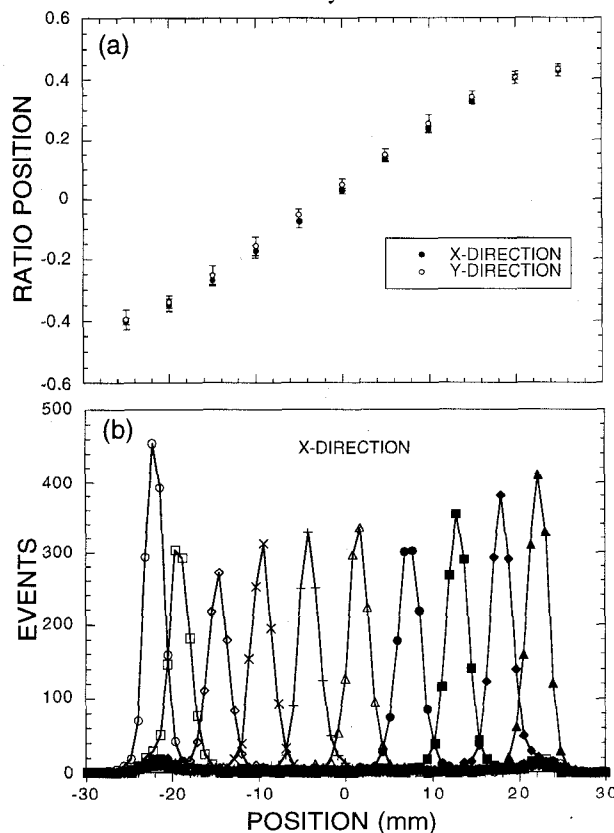


Figure 2. Imaging results from the small NaI(Tl)-PSPMT gamma camera. (a) the x and y ratio positioning response (LSF peak position) vs. position of a ~ 1.2 mm slit source of ⁵⁷Co stepped across the camera FOV in 5 mm steps; (b) the x-direction LSFs corresponding to the data plotted in (a).

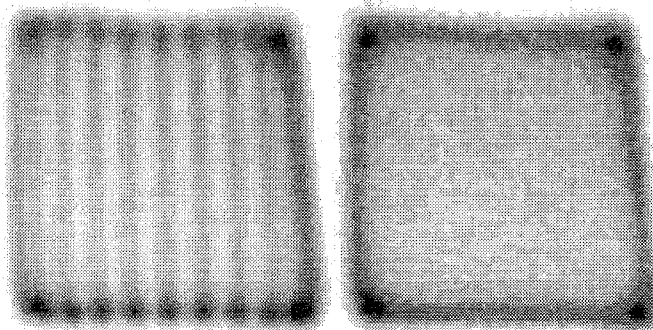


Figure 3. Left: sum of the images used to obtain x-LSFs in Figure 2b (without flood correction). Right: flood field image. Image Scale: Darkest = Highest Counts.

superior to that measured in standard nuclear medicine gamma cameras (>3.5 mm FWHM intrinsic resolution).

Figure 3 shows the sum of the line images used to obtain the x-direction LSFs of Figure 2b (without flood correction) and the corresponding flood field image. The flood image shows the presence of hot spots on the image borders due to background from scattered gamma rays and noise. Within the inner, most linear 5 cm x 5 cm FOV, the standard deviation (σ) of the pixel intensity values in the flood image is 21% of the mean. The cause of the slant distortion in the upper right hand corner of the images is due to a NaI(Tl) package defect.

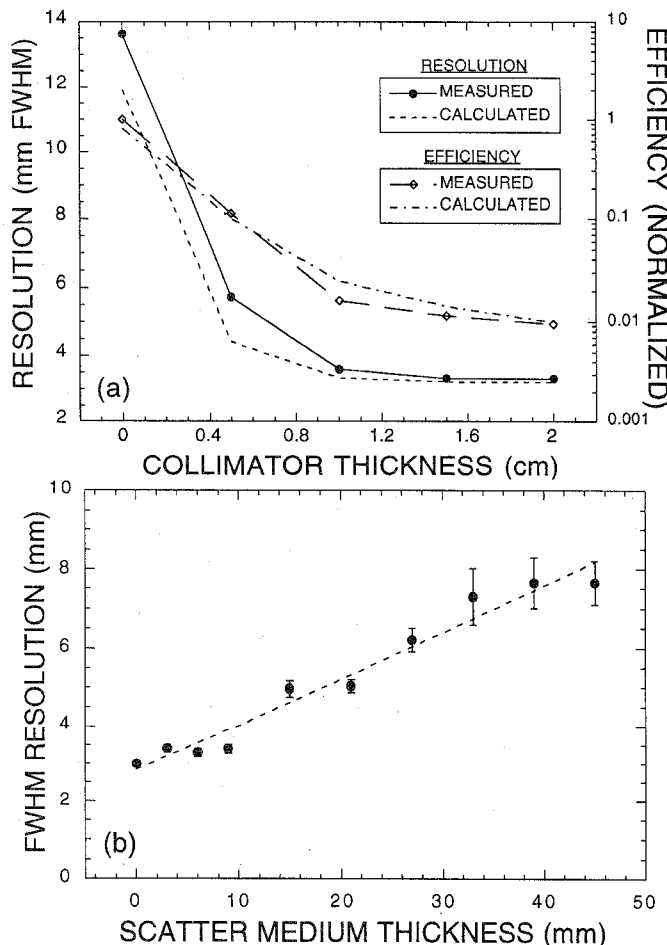


Figure 4. (a) Resolution and efficiency vs. collimator thickness for NaI(Tl)-PSPMT. Both measured and calculated values are shown. (b) Resolution vs. cold scatter medium (Lucite sheets) thickness (for 2.0 cm thick collimator). A ^{57}Co point source at center of FOV was used for the measurements.

Figure 4a shows the resolution and efficiency vs. length of the lead collimator holes used on the NaI(Tl)-PSPMT device. The measured values were obtained with a ^{57}Co point source on top of the collimator at the camera center. The calculated resolution values comprise the square root of the sum of the squares of the calculated collimator resolution (from a formula in ref.[26]) and measured intrinsic detector resolution (2.5 mm FWHM) components. The collimator hole diameter was approximately 1.3 mm and the septa thickness was roughly 0.16 mm. Results in Figure 4a indicate that it may be possible to use less than a 2.0 cm thick collimator, preserving sensitivity without much loss in resolution. The measured point source sensitivity at the center of the crystal, without the collimator, was approximately 4×10^4 counts/sec/ μCi . With the 2.0 cm thick collimator the corresponding value was ~ 400 cts/sec/ μCi . As seen from the figure, both the measured resolution and efficiency data compare well to that calculated using the standard collimator formulas for resolution and efficiency vs. hole length [26].

Figure 4b displays the measured image resolution (FWHM) of a ^{57}Co point source within a tissue equivalent scatter medium (Lucite sheets) of varying thickness. This simulates imaging a hot tumor within a cold compressed breast of different thickness. The blurring with thickness is due to both scatter and the $1/r^2$ effect. For all depths within scatter medium studied, the point source is clearly resolved.

Figures 5 and 6 show the high resolution imaging capabilities of the NaI(Tl)-PSPMT camera. Figure 5 (left) displays the digitized transmission phantom (scale shown). Recall the letters have nominally 1.5 mm line widths (with some variation). Figure 5 (right) shows the corresponding transmission image acquired using $^{99\text{m}}\text{Tc}$, without flood correc-

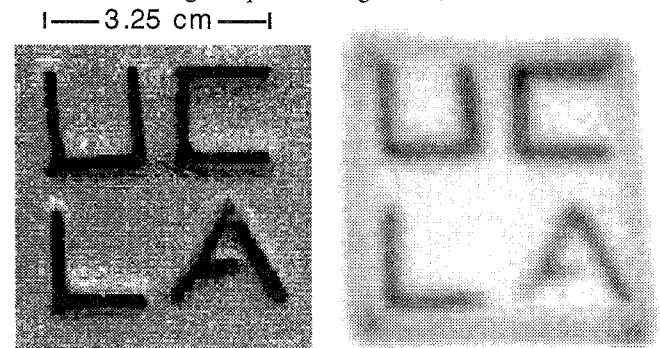


Figure 5. Left: Digitized transmission phantom (scale shown) with nominally 1.5 mm line widths. Right: The corresponding $^{99\text{m}}\text{Tc}$ transmission image acquired with NaI(Tl)-PSPMT camera.

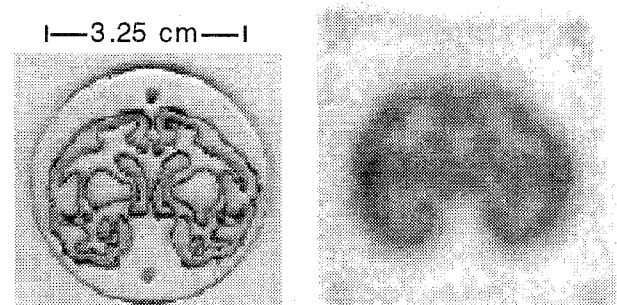


Figure 6. Left: Digitized small brain phantom (scale shown) contains fine structures. Right: the NaI(Tl)-PSPMT camera (with 2.0 cm thick collimator) has capability of resolving some of the fine structures when the phantom is filled (inside black bordered regions) with $^{99\text{m}}\text{Tc}$ (darkest regions have highest counts). Image is shown without flood correction or energy thresholding.

tion or energy thresholding. Figure 6 (left) shows the digitized small monkey brain phantom (scale shown) and (right) demonstrates that NaI(Tl)-PSPMT camera with a 2 cm thick collimator is able to resolve some of the fine structures of this small phantom (^{99m}Tc inside black bordered regions) with good linearity. Again, no energy thresholding was used.

Figure 7 shows some of the results obtained with discrete crystal arrays coupled to the PSPMT. ^{99m}Tc flood irradiation histograms are displayed for arrays of (a) $2 \times 2 \times 6 \text{ mm}^3$ NaI(Tl) crystals spaced 0.5 mm apart and (b) $2 \times 2 \times 4 \text{ mm}^3$ CsI(Tl) crystals spaced 0.5 mm apart. Below each image is the extracted energy spectra from the crystal in row 2 and column 2 of each array (without gain corrections applied to the 4 PSPMT readout channels). An absolute comparison between the two energy spectra results is difficult since there is a 3 mm glass window on the NaI(Tl) array, but not on the CsI(Tl) array, which was directly coupled to the PSPMT (resulting in better light transmission). Cs or I escape x-rays results in a low energy asymmetry seen on the photopeaks.

The bottom graph of Figure 7 shows the results of stepping the 4×4 NaI(Tl) array across the PSPMT in 10 mm steps. We plot the ratio positioning response (crystal peak position in image) vs. actual crystal position for all array positions. The linearity and dynamic range appear to give a

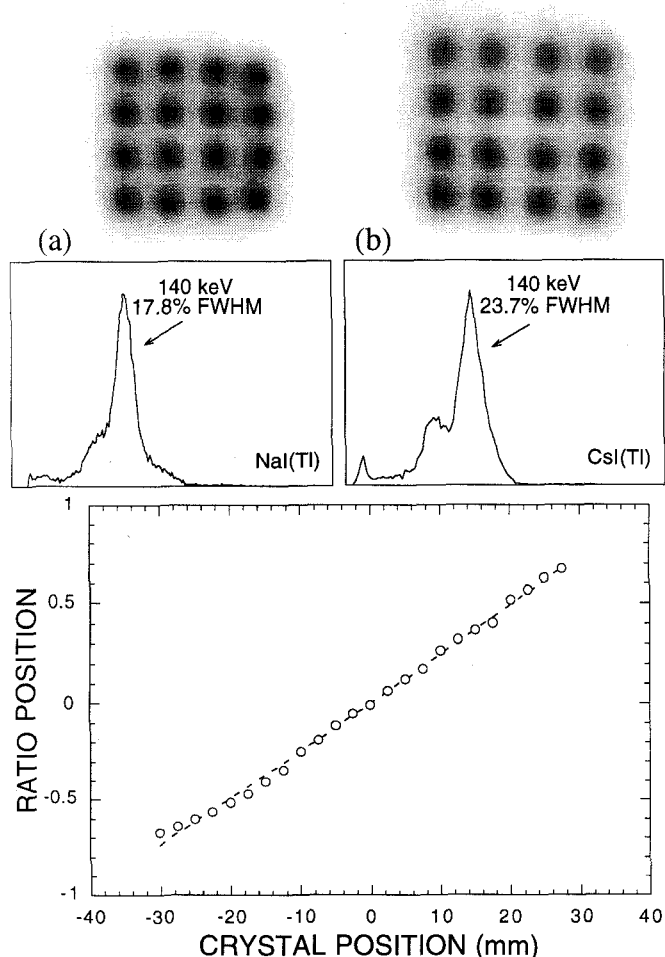


Figure 7. Top: ^{99m}Tc flood histograms of arrays of (a) $2 \times 2 \times 6 \text{ mm}^3$ NaI(Tl) and (b) $2 \times 2 \times 4 \text{ mm}^3$ CsI(Tl) crystals spaced 0.5 mm apart. Below each image is the extracted energy spectra from the crystal in row 2 and column 2 of each array (without gain corrections applied to the tube). Bottom: The ratio positioning response for each crystal position in the 4×4 NaI(Tl) array when it is translated across the PSPMT in 10 mm steps.

central $6 \times 6 \text{ cm}$ FOV, which is an improvement over the continuous crystal (see Fig. 2a, for comparison and the end of Section IIA). Imaging with the discrete array is accomplished by determining which crystal is hit and placing the event at that crystal location. A digital positioning mask made of the horizontal and vertical crystal borders in the flood image facilitates the decision of which crystal is hit. Results from position measurements made with crystal arrays indicate that the intrinsic position resolution is determined by the size of the crystals in the array.

B. The PD Camera Simulations, Energy Measurements and Positioning Studies

Figure 8 displays some of the Monte Carlo results for the continuous crystal CsI(Tl)-photodiode design (Fig. 1a). The top of Figure 8 shows Monte Carlo simulations of scintillator light spread (FWHM and FWTM) for a point source of light at the center of a CsI(Tl) crystal as a function of light diffuser thickness. For a 4 mm thick light guide, the predicted FWHM spread, ($\sim 11 \text{ mm}$) is roughly the size of the proposed photodiode spacing, which is appropriate for event positioning. The bottom of Figure 8 shows results of Monte Carlo simulations of intrinsic position resolution (fluctuation in scintillation event positioning) as a function of depth with-

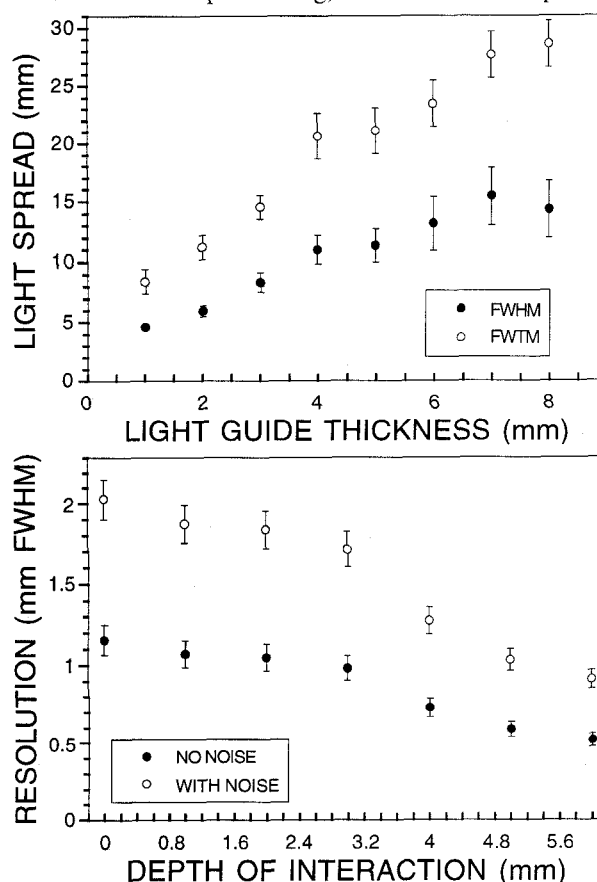


Figure 8. (Top) Monte Carlo simulations of scintillator light spread (FWHM and FWTM) for a point source of light at the center of a CsI(Tl) crystal as a function of light diffuser thickness for the design of Figure 1a. (Bottom) Monte Carlo simulations of intrinsic position resolution vs. depth within crystal of a point source origin of light. Resolution is predicted with and without estimated weighted mean positioning errors due to photodiode noise and size. A 4 mm thick light diffuser was assumed.

in the crystal of a point source origin of light (depth of interaction). Resolution is predicted with and without estimated weighted mean positioning errors due to photodiode noise (450 electrons RMS assumed) and size (10 mm) error propagation. Only the local 3x3 PDs surrounding the light source position were used for the weighted mean calculation (a.k.a. "local centroid"). We see from the figure that intrinsic resolution better than 2.0 mm FWHM is expected at the center for all depths of interaction. The attainable system resolution will, of course, be further limited by the collimator properties.

Figure 9 shows a typical energy spectrum measurement for the proposed CsI(Tl)-PD combination (1 cm² PD). We fit the measured photopeak to a single gaussian (which may be inappropriate for ⁵⁷Co data because of a higher energy line at 136 keV and the presence of the ~90 keV x-ray escape peak, as seen in Fig. 7). An energy resolution of 23%, 8.9% and 7.6% FWHM was measured for the 122, 511, and 662 keV lines of ⁵⁷Co, ²²Na and ¹³⁷Cs sources, respectively. The ⁵⁷Co gamma ray energy is similar to that emitted from ^{99m}Tc. Due to the good match between the CsI(Tl) emission and silicon absorption spectra, relatively good energy resolution characteristics are measured even in the presence of a PD dark current of 2-5 nA and a terminal capacitance of 40 pf. These results would greatly improve with a reduced photodiode area.

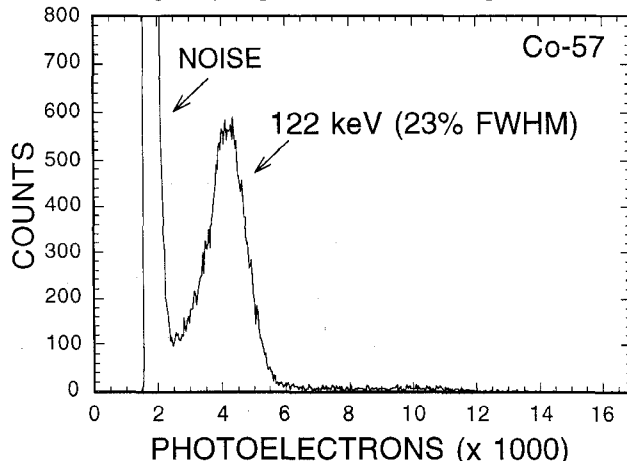


Figure 9. Energy spectrum measured with a 2x2x10mm³ CsI(Tl) crystal, a 1cm² PIN photodiode, and a ⁵⁷Co gamma ray source.

We performed an approximate charge calibration using direct interactions of 59.5 keV ²⁴¹Am x-rays in the silicon. The electronic noise contribution for this PD-preamplifier combination was determined to be approximately 450 electrons RMS using the electronic pulser test input of the preamp. The ⁵⁷Co 122 keV peak corresponds to roughly 4200 photoelectrons. Assuming a photodiode quantum efficiency of roughly 75%, this is equivalent to 5600 scintillation photons input to the PD. A 122 keV gamma ray interaction in CsI(Tl) should produce ~6300 scintillation photons, so that we are collecting ~89% of the available scintillation light. This fraction compares well to that calculated from DETECT Monte Carlo photon tracking studies. The 122 keV peak channel in Figure 9 is nearly twice the top channel of the noise shoulder.

Figure 10 shows a schematic of the 1-D experimental set-up used to measure positioning response of a continuous CsI(Tl) crystal coupled to 2 PDs. The crystal was 25 mm x 25 mm in area, 4 mm thick, and the sides and top were covered with a white teflon reflector. The photosensitive area of each PD is 10mm x 10mm with a ceramic packaging approximate-

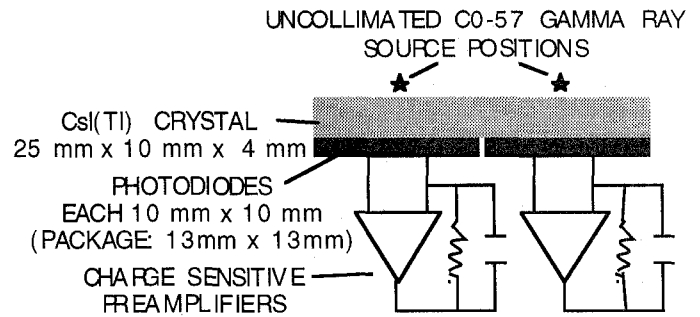


Figure 10. Schematic of 1-D experimental set-up to measure positioning response of a large CsI(Tl) crystal coupled to 2 PDs. The noise conditions were less than ideal.

ly 12.7 mm x 12.7 mm. An uncollimated ⁵⁷Co (122 keV) gamma ray source was placed at two separate positions in line with the center of each PD, as shown.

The noise conditions of this test set-up (Fig. 10) were less than ideal for position measurements. The two different charge sensitive preamplifiers ORTEC models 142A (Channel 1) and 109A (Channel 2) of the test set-up had different noise characteristics as seen in the top spectra shown in Figure 11, measured separately with a small CsI(Tl) crystal on either photodiode ("isolated readout") (compare with Fig. 9). The energy resolution of the 122 keV photopeak was roughly 32% better for the 142A than for the 109A channel. In addition, it was not possible to mount the photodiodes directly on the preamplifier input connectors and so twisted pair wires approximately 10 cm long were used to make the connection for each channel. This increase in stray input capacitance degraded the individual energy resolutions. There was also some small amount of crosstalk between the two closely packed ("coupled readout") PD channels, compared to when they were isolated from each other. Thus, the resulting SNR with the positioning test set-up (bottom plots of Figure 11) was significantly worse than (1) when the two channels were isolated (compare top and bottom spectra) and (2) that expected in the actual system proposed where, ideally, the PD leads would be mounted directly onto the preamp input FET. This degradation in energy response will directly lead to positioning response degradation. Finally, because of the small size of the

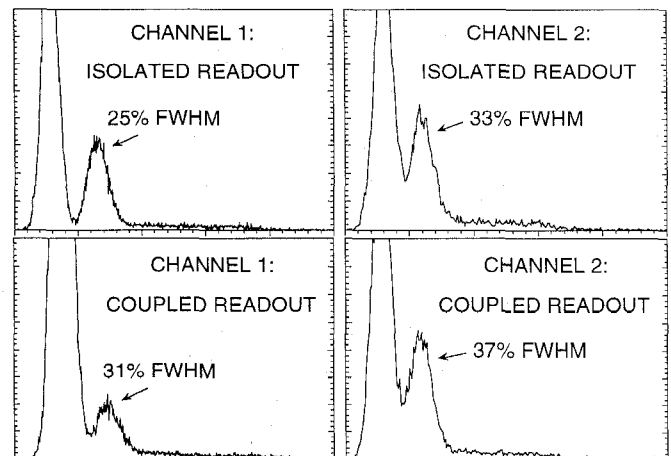


Figure 11. ⁵⁷Co CsI(Tl)-PD energy spectra measurements using the two preamps. Top: Each PD is mounted directly on the preamp input connector and isolated from the other channel. Bottom: The two powered PDs and preamps are coupled as close together as possible as shown in Fig. 10. The energy resolution in the bottom spectra is degraded compared to the top.

crystal in the test set-up, "edge effects" inherent to standard scintillation imaging, are most likely present for all positions within the crystal.

Even with these shortfalls we have some preliminary positioning results with this test CsI(Tl)-PD set-up of Figure 10. Figure 12 displays a histogram of the normalized weighted mean of the two PD signals from an event (position = difference divided by sum, a.k.a. "ratio position") measured separately for two uncollimated source positions (displayed on the same graph) for the configuration shown in Figure 10. Even though the noise conditions were less than ideal, the two source positions are well resolved. The resolution of the ^{57}Co measurement was 4.9 mm FWHM for the left source position and 5.1 mm for the right (the right PD was readout by the "noisier" preamp). These results represent the worst case scenario, and performance characteristics, such as resolution and dynamic range, are expected to improve significantly with proper low noise readout of the two PD channels, collimation of the gamma rays and proper size crystal and crystal surface treatments. From the Monte Carlo study results described earlier in this section, if we can achieve 450 electrons RMS noise for all PD channels, we should be able to achieve 2 mm resolution FWHM for a collimated point source at the center of a 6 cm x 6 cm x 6 mm thick crystal.

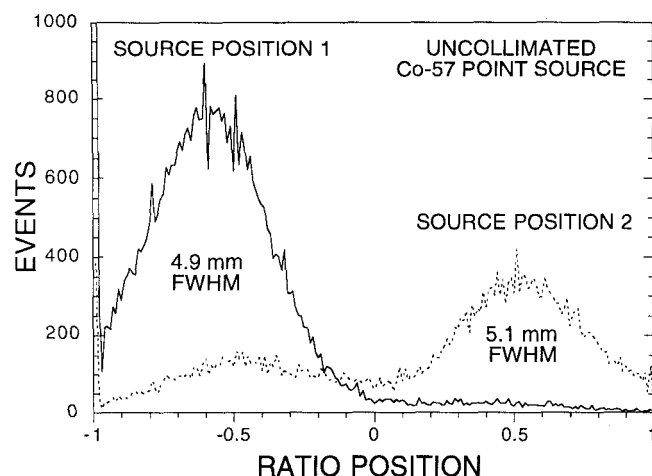


Figure 12. Preliminary positioning results with the test set-up shown in Figure 10 using an uncollimated ^{57}Co point source. Histogram of the normalized weighted mean of the two PD signals from an event (position = difference divided by sum) measured separately for two uncollimated source positions (displayed on the same graph). The two source positions were well resolved even though the noise level was significantly higher than anticipated in the proposed system.

IV. SUMMARY

A small scintillation camera may be very useful in imaging the breast because it allows for optimum camera positioning and can take advantage of the use of breast compression. Both of these properties allow for a reduction of background radiation. We have considered two possible photodetector technologies for the small camera: the position sensitive PMT (PSPMT) with NaI(Tl), and the silicon PIN photodiode(PD) with CsI(Tl). The former has the advantage in terms of intrinsic noise and gain. The latter has an advantage in terms of compactness and eventual cost.

We have achieved average intrinsic resolution of 2.2 mm FWHM (source size deconvolved) with the PSPMT scheme.

This value is better than that usually achieved with a standard scintillation camera because of the smaller effective spacing between photodetectors (anode wires) [27] and favorable geometry of the PSPMT. We have seen that there is reasonable spectral resolution for the PD design and that good positioning results are expected even factoring in the uncorrelated PD noise from the PDs involved in the weighted mean calculation. In a noisy test experiment with two channels, there was adequate signal-to-noise ratio for 122 keV gamma ray event positioning. However, significant work is required before high resolution positioning is possible. It may be necessary to reduce the PD pixel size for lower noise.

Good energy resolution is important for scatter rejection for the small scintillation camera. Scatter rejection is important for restoring image contrast, allowing for better lesion detection. We will make efforts to improve our energy resolution results for the PSPMT and the PD designs. We expect that the scatter fraction from the body will be lower for our small camera geometry and protocol than for a standard nuclear medicine gamma camera study since we will shield the sides of the small camera and image the breast from either the superior or inferior position. This will reduce scatter into the relatively small FOV. Future studies will include tumor phantom studies with various activity concentration ratios between tumor and background which will allow us to ascertain the importance of scatter rejection. We will also make a more detailed comparison between the discrete and continuous crystal geometries, and try to improve the dynamic range and resolution of the PSPMT readout.

V. ACKNOWLEDGMENTS

This work was supported in part by funds provided by the Breast Cancer Fund of the State of California through the Breast Cancer Research Program of the University of California, Grant Number IRB-0225, the Department of Energy (DE-FCO3-87-ER 60615), National Institutes of Health (RO1-CA61037), and a pilot research grant from the Society of Nuclear Medicine Education and Research Foundation.

VI. REFERENCES

- [1] I Khalkhali, et al. "Tc-99m-SestaMIBI Prone Imaging in Patients (PTS) with Suspicion of Breast Cancer (Ca)", *J. Nucl. Med.*, 24:140P, May 1993.
- [2] CJ Baines, et al. "Sensitivity and specificity of first screen mammography in the Canadian National Breast Screening Study: a preliminary report from five centers". *Radiology*, 160:295-298, (1986).
- [3] L Tabar et al. "Mammographic parenchymal patterns: risk indicator for breast cancer?" *JAMA* 247:185-189, (1982).
- [4] S Piccolo, et al. "Technetium-99m-Methylene Diphosphonate Scintimammography to Image Primary Breast Cancer." *J. Nuc. Med.* 1995. 36:718-724.
- [5] I Khalkhali, et al. "Clinical and Pathologic Follow up of 100 Patients with Breast Lesions Studied with Scintimammography." *J. Nuc. Med.* 35:22P, 1994.
- [6] Lastoria, P. Varrella, C Mainolfi, E. Vergara, S. Maurea, et al. "Tc-99m Sestamibi Scintigraphy in the Diagnosis of Primary Breast Cancer." *J. Nuc. Med.* 35:22P, 1994.
- [7] A Waxman, et al. "Sensitivity and Specificity of Tc-99m Methoxyisobutyl Isonitrile (MIBI) in the Evaluation of Primary Carcinoma of the Breast: Comparison of Palpable and Non-palpable Lesions with Mammography." *J. Nuc. Med.* 35:22P, 1994.

- [8] I Khalkhali, et al. "Tc-99m-Sestamibi Scintimammography of Breast Lesions: Clinical and Pathological Follow-up." *J. Nuc. Med.* 36:1731, Oct. 1995.
- [9] R Taillefer, et al. "Technetium-99m-Sestamibi Prone Scintimammography to Detect Primary Breast Cancer and Axillary Lymph Node Involvement." *J. Nuc. Med.* 36: 1758, Oct. 1995.
- [10] J. Maublant, M. de Latour, M. Mestas et al. "Technetium-99m-Sestamibi Uptake in Breast Tumors and Associated Lymph Nodes." *J. Nucl. Med.* 37-6:922-925, June 1996.
- [11] J. Villanueva-Meyer, M.H. Leonard Jr. et. al. "Mammoscintigraphy with Technetium-99m-Sestamibi in Suspected Breast Cancer." *J. Nucl. Med.* 37-6:926-30, June 1996.
- [12] H.O. Anger. "Scintillation Camera." *Rev. Sci. Instr.* 29(1), 27-33 (1958).
- [13] C.J. Thompson, K. Murthy et.al. "Feasibility Study for Positron Emission Mammography." *Med. Phys.* 21(4): 529-38, (1994). "Positron Emission Mammography (PEM): A Promising Technique for Detecting Breast Cancer." *IEEE Trans. Nucl. Sci.*, 42-4:1012-7 (1995).
- [14] W.W. Moses, T.F. Budinger, R.H. Huesman and S.E. Derenzo. "PET Camera Designs for Imaging Breast Cancer and Axillary Lymph Node Involvement." *J. Nucl. Med.* 36-5:69P, May 1995.
- [15] G.D. Hutchins and A.J. Simon. "Evaluation of Prototype Geometries for Breast Imaging with PET Radiopharmaceuticals." *J. Nucl. Med.* 36-5:69P, May 1995.
- [16] B.E. Patt, J.S. Iwanczyk, Y.J. Wang, M.P. Tornai, C.S. Levin, E.J. Hoffman. "Mercuric Iodide Photodetector Arrays for Gamma-Ray Imaging." *Nucl. Inst. & Meth. A* 1996 (in press).
- [17] J.N. Aarsovold, H.H. Barrett, et. al. "Modular scintillation cameras: a progress report." *Proc. SPIE.* 914(A):319-25.
- [18] A.J. Bird, et.al. "Multi-channel readout of crossed wire anode photomultipliers." *Nuc. Inst. Meth.* A348(2-3):668-72 (1994).
- [19] N.J. Yasillo, R.N. Beck, M. Cooper. "Design considerations for a single tube gamma camera." *IEEE Trans. Nucl. Sci.* 37(2):609-15 (1990).
- [20] Weisenberger, A.G.; Majewski, S.; Mehrotra, S.; Popov, V.; and others. Investigation into the use of position sensitive photomultiplier tubes for beta radiography. 1994 IEEE Nucl. Sci. Symp. Conf. Rec 1:351-5 (1995).
- [21] E. Rossi, C. Labanti, et al. "A hexagonal multi-element CsI(Tl)-photodiode module for gamma-ray imaging." 1995 Conf. Rec. IEEE Nuc. Sci. Symp. 1:60-64 (1995).
- [22] T. Carter et al. "An imager prototype for gamma-ray astronomy." 1994 IEEE Nucl. Sci. Symp. Conf. Rec. 1:56-59 (1995).
- [23] C.S. Levin, E.J. Hoffman, M.P. Tornai, L.R. MacDonald. "Design of a Small Scintillation Camera with Photodiode Readout for Imaging Malignant Breast Tumors." *J. Nucl. Med.* 37, p. 52, May 1996.
- [24] GF Knoll, TF Knoll, TM Henderson. "Light Collection in Scintillating Detector Composites for Neutron Detection." *IEEE Trans. Nucl. Sci.* NS-35(1):872-5 (1988).
- [25] FD Rollo, Ed. *Nuclear Medicine Physics, Instrumentation, and Agents.* C.V Mosby Company. St. Louis, 1981. Ch. 6.
- [26] J.A. Sorenson and M.E. Phelps. *Physics in Nuclear Medicine.* W.B. Saunders Co., Philadelphia, 1987, Ch. 16.
- [27] E Tanaka, T Hiramoto, N. Hohara. "Scintillation Cameras Based on New Position Arithmetics." *J. Nuc. Med.* 11(9):542-7(1970).